ADVANCED ENGINEERING MATERIALS
www.aem-journal.com

Stress Reduction of 3D Printed Compliance-Tailored Multilayers

Shanmugam Kumar, Brian L. Wardle, Muhamad F. Arif, and Jabir Ubaid*

Multilayered multi-material interfaces are encountered in an array of fields. Here, enhanced mechanical performance of such multi-material interfaces is demonstrated, focusing on strength and stiffness, by employing bondlayers with spatially-tuned elastic properties realized via 3D printing. Compliance of the bondlayer is varied along the bondlength with increased compliance at the ends to relieve stress concentrations. Experimental testing to failure of a tri-layered assembly in a single-lap joint configuration, including optical strain mapping, reveals that the stress and strain redistribution of the compliance-tailored bondlayer increases strength by 100% and toughness by 60%, compared to a constant modulus bondlayer, while maintaining the stiffness of the joint with the homogeneous stiff bondlayer. Analyses show that the stress concentrations for both peel and shear stress in the bondlayer have a global minimum when the compliant bond at the lap end comprises ≈10% of the bondlength, and further that increased multilayer performance also holds for long (relative to critical shear transfer length) bondlengths. Damage and failure resistance of multi-material interfaces can be improved substantially via the compliance-tailoring demonstrated here, with immediate relevance in additive manufacturing joining applications, and shows promise for generalized joining applications including adhesive bonding.

1. Introduction

Highly heterogeneous materials with variable and functionally graded local compliance are widespread in nature. Emulating these natural material solutions, engineering graded materials that are stronger and more damage-resistant than their conventional homogeneous counterparts are of great interest. Grading is particularly important at the interfaces between dissimilar materials, where failure commonly originates.[1–6] With the advent of various technologies to synthesize and process materials in 3D, gradations in composition, structure, and properties may now be practically engineered over a wide range of length scales ranging from nanometers to meters.[3,5,7] Such grading, either continuous or in ever-finer, discrete steps, across an interface and between two dissimilar materials, has been used to redistribute thermal stresses,[8] thereby limiting the stresses at critical locations and thus suppressing the onset of permanent (plastic) deformation, damage, or cracking.[9–11] Grading of composition is particularly beneficial at mechanical interfaces between dissimilar materials, where stress and strain jumps naturally arise due to mismatch in elastic properties.[12–16] A particularly important engineering application of such grading of interfaces is in multilayers.

Multilayers composed of either similar or dissimilar materials, experience stress, and strain concentrations at the ends of the overlap, where such assemblies fail. The stress and strain concentration is particularly problematic in single-lap joint (SLJ) configurations (see **Figure 1**a) due to the eccentric load path that introduces bending moments and transverse shear forces into the joint (see Figure S1). Goland and Reissner[12] is noted as the first to account for the rotation of the joint due to such load path eccentricities and provided analytical expressions for both shear and peel stress concentrations in the bondlayer. To minimize the deleterious effect of such stress concentration on the performance of joints, several techniques have been proposed, among which geometrical grading such as stepping or tapering of the adherends (e.g., see ref.[13,14]) modification of the bondlayer geometry (e.g., see ref.[15]) and employing a bead at the lap ends of the bondlayer (called a "spew geometry" e.g., see ref.[16,17]) were found to be marginally effective and have numerous limitations restricting their application in practice due to producibility constraints, for example.[18] Therefore, a few studies have employed more compliant bondlayers in order to minimize the (most problematic) peel stresses. However, with this approach, the increase in strain-tolerance is achieved at the expense of reduced strength and stiffness of the joint. Moreover, a more compliant bondlayer also requires a longer bondlength to enable shear-dominated load transfer across the bondlayer and accommodation of such a longer bondlength is not always feasible.

Prof. S. Kumar, Dr. M. F. Arif, J. Ubaid
Department of Mechanical and Materials Engineering
Khalifa University of Science and Technology, Masdar Institute,
Masdar City, P.O. Box 54224, Abu Dhabi, UAE
E-mail: s.kumar@eng.oxon.org; skumaar@mit.edu

Prof. B. L. Wardle
Department of Aeronautics and Astronautics
Massachusetts Institute of Technology, Cambridge, MA 02139, USA

The ORCID identification number(s) for the author(s) of this article can be found under https://doi.org/10.1002/adem.201700883.

DOI: 10.1002/adem.201700883

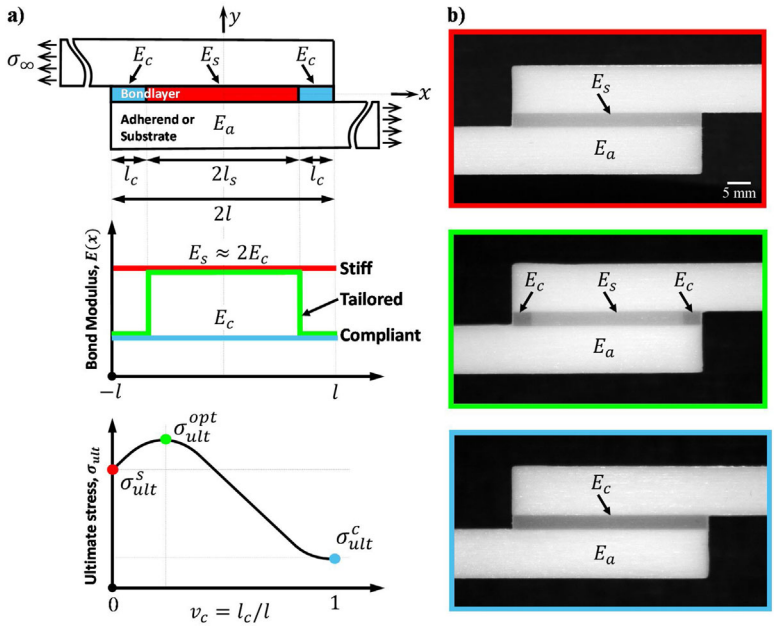

Figure 1. Compliance-tailored tri-layer single-lap joints (SLJs): a) Conceptual representation of SLJ subjected to a far-field tensile stress σ_∞ with different bondlayer modulus profiles. Bottom shows the ultimate stress (σ_{ult}) for constant modulus bondlayers (either E_s or E_c) and compliance-tailored systems as a function of volume fraction of compliant bond $v_c = l_c/l$; b) Optical images of 3D printed SLJs with bondlayer compliance-tailoring considering all three profiles in a), including homogeneous stiff ($v_c = 0$) and compliant ($v_c = 1$), and tailored ($v_c = 0.2$) cases. Scale bar in b) is not repeated in remainder of manuscript.

Spatially tailoring the elastic properties of the bondlayer along the bondlength to reduce end stress and strain concentrations began with the pioneering theoretical studies of Raphael,[19] Hart-Smith,[20] and Srinivas.[21] That work showed that the peel and shear stresses in the bondlayer could be reduced significantly by using a combination of flexible and stiff bonds. Recently, there is growing interest in this area due to the ability to experimentally realize such systems[5,22,23] through both micro- and nano-engineering, while theoretical studies have considered compliance-tailoring of the bondlayer along the bondlength providing a general framework for the stress and strain analysis of bonded systems (e.g., see ref.[24–28]). Here, we explore a step-wise compliance-tailored SLJ configuration using a bi-modulus bondlayer to realize experimentally enhanced performance of the assembly. Via 3D printing, tailored bondlayers are realized with a stiffer bond in the middle portion of the bondlength. The compliant bond at the overlap ends imparts strain-tolerance, while the stiff bond maintains efficient load transfer by redistributing both the peel and shear stresses over the bondlength, thus reducing the concentrations at the ends of the overlap, where failure emanates. Via optical strain mapping and finite element analysis (FEA), the stress and strain redistributions are shown to impart increased performance of the multi-layer assembly (as a function of volume fraction of compliant bond in the bondlayer), improving performance across all the relevant metrics including strength, load transfer efficiency, stiffness, toughness, and deflection to break.

2. Experimental Section

Additive manufacturing to realize compliance-tailored bondlayers in the multi-material SLJ system is discussed, followed by experimental methods of joint testing including optical strain mapping.

3D Printing and Compliance-Tailoring of the Multimaterial Joint

We utilize Polyjet photopolymer technology that allows multi-material deposition[29–32] to 3D print compliance-tailored single-lap joints (SLJs), as shown in Figure 1a (top). The emergence of such multi-material and composite 3D printing technologies[33–39] facilitates the design of functionally graded designs at the sub-millimeter scale enabling fabrication of multi-material structures simultaneously exhibiting both strength and toughness, which are often difficult to achieve with homogeneous materials.[40,41]

CAD models of SLJs were created using Solidworks (Dassault Systemes, France) and an Object Connex260 Polyjet 3D printer (Statasys Ltd., USA), having eight simultaneously operating print heads, was used for fabrication. The tool has resolution of 16 µm in the z-direction (width of joint) and 42 µm in the x- and y-directions (see Figure 1a, top). The printing direction is known to influence the material behavior of printed specimens,[38,42] although this is not relevant in the comparisons here. The liquid photopolymers are cured by UV light concurrent with deposition, producing a fully cured, fully dense structure with no measurable porosity. The ability of this printer to co-deposit two different polymers (enabling what are termed "digital materials") is utilized in this work to create bondlayers with differing properties, principally moduli. Two basic polymers, namely VeroWhitePlus™ RGD835 (relatively stiff polymer) and TangoPlus FLX930 (relatively compliant polymer) were employed. The adherends were 3D printed using a VeroWhitePlus™ RGD835, having a Young's modulus (E_a) of 2114 MPa. The bondlayer was printed using "digital material" S40 (a co-deposition of VeroWhite and TangoPlus) having Young's modulus $E_c = 1.09$ MPa for the compliant bondlayer, and S60 having Young's modulus $E_s = 2.48$ MPa for the stiff bond. See discussion and Figure S3 for the constitutive properties of these three different materials, noting that $E_a \gg E_s \cong 2E_c$. The different configurations tested are shown in Figure 1b, and include both stiff and compliant constant modulus bondlayers, and bi-modulus compliance-tailored bondlayers of different length fractions, v_c. The geometric details of the compliance tailored joints are shown in Figure S2 with $2l = 40$ mm, $w = 20$ mm. l_c and l_s are the length of the compliant and stiff bonds, respectively. SLJs for each volume fraction of compliant bond $v_c = \{0, 0.2, 0.4, 0.6, 0.8, 1.0\}$ were 3D printed and tested under monotonic tension until failure. A support material (Objet Support SUP705) was used during printing to enable fabrication

of overhang portions of geometries and was subsequently removed through water washing.

Mechanical Testing

The 3D printed joints were tested in a Zwick-Roell tensile testing machine with a 2.5 kN load cell. The load cell accuracy is $<\pm 0.25\%$ for the measurement range of 10–2500 N, and $<\pm 1\%$ for the measurement range of 2.5–10 N. The tensile load was applied at a constant crosshead speed of 5 mm min^{-1} and displacement was measured at the grips with a travel resolution of 0.041 µm. Digital image correlation (DIC) was used for full-field measurement of shear and peel strains in the joint as a function of load using a monochrome 5.0 MP camera. Random white/black speckle patterns of acrylic paint were formed on the specimen's surface using an airbrush prior to testing. Vic-2D software was used to evaluate the evolution of the strain field as a function of load. Each of the bondlayer designs was tested three times to evaluate repeatability.

3. Finite Element Analysis

The SLJ asemblies are modeled as a plane-strain problem to reduce computational effort, utilizing a commercial finite element code, Abaqus/Standard FEA version 6.12. The geometric model represents the experimental study, except in the case of the later analysis where the bondlength $2l$ is increased, and the linear elastic material constants used are obtained from our own material characterization experiments (see Figure S3 and related discussion). The model is meshed using a bilinear plane-strain quadrilateral element (CPE4). The element size for the bondlayer is chosen by carrying out a mesh convergence study following usual practice.[43] With a mesh size lower than 375 µm, the peel and shear stress distributions at the bondlayer mid-surface do not change more than 2% with further reduction in mesh size. It should be noted that the stress field at the bondlayer-adherend interface near the free edges of the bondlayer is more sensitive to mesh size reduction due to the presence of a singularity at the bondlayer-adherend free edge junction.[23] Since the aim of this study is not to capture the singular stress field, but to compare the stress field in different compliance-tailored systems, an average mesh size of 187.5 µm (16 elements across bondlayer thickness) is used for the bondlayer while a coarser mesh (500 µm) is used for the region of adherends away from the bondlayer (see Figure 4a). The vertical edge of left hand side adherend is constrained in the x-direction and a far-field tensile stress σ_∞ is applied to the right hand adherend. Over a small length of adherends (as shown in Figure 4a), vertical displacement (y-direction) is constrained to simulate grip boundary conditions. FE model is benchmarked with the experimentally observed mechanical response of the compliance-tailored joints (see Figure S4 and related discussion).

4. Results and Discussion

The load–displacement response of SLJs with different compliant-to-stiff bondlength ratio (or volume fraction of the compliant bond in the bondlayer), $\nu_c = l_c/l$ (see Figure 1a,b), under quasi-static tension is shown in **Figure 2**a. Joint stiffness trends are as expected: the joint with stiff bondlayer ($\nu_c = 0$) has nearly double the stiffness of the compliant bondlayer joint ($\nu_c = 1$). Introduction of more compliant bond (recall $E_s \cong 2E_c$) at the ends of the bondlayer improves the joint performance broadly (see Figure 2 and **Table 1**). Taking joint strength as an example, increasing ν_c improves the joint strength versus the stiff bondlayer joint, but the performance starts decreasing beyond a particular ν_c and approaches that of the compliant bondlayer joint ($\nu_c = 0$), as shown in Figure 2b. For a given set of geometric and material parameters, there exists an optimal ν_c (near 0.2 in this case) for strength, due to stress and strain redistribution and reduction of the concentrations at the joint end. Table 1 provides the summary of performance of the constant modulus and tailored SLJs. Changes (shown in red) are calculated versus both the stiff and compliant constant modulus bondlayer joints. The highest strength SLJ realized experimentally, at $\nu_c = 0.2$, is noted to be improved relative to both constant modulus cases across all the joint performance metrics: beyond the large strength increases, joint toughness and deflection at break are increased, while maintaining the joint stiffness of the (stiffest) constant modulus bondlayer assembly, *i.e.*, across all relevant metrics, the $\nu_c = 0.2$ tailored joint is higher performing. Interestingly, several prior studies[44–46] demonstrated experimentally that a tailored joint can significantly outperform a constant modulus stiffer joint, but has only marginal merit compared to a (more) compliant joint. Our work shows significant improvements in both constant modulus cases with statistical significance.

Figure 3 shows the strain distributio n in the joint region obtained from digital image correlation at a load level of 300 N (in the pre-dominantly linear elastic region for all the joints (see Figure 2a) for different ν_c. The first row in Figure 3 is for the case of stiff bondlayer joint ($\nu_c = 0$), the bottom row is for the compliant bondlayer joint ($\nu_c = 1$) and the middle row is for the highest-performing compliance-tailored bondlayer joint ($\nu_c = 0.2$). Both shear and peel strains are relatively high in the compliant joint as expected (the bottom row of Figure 3)

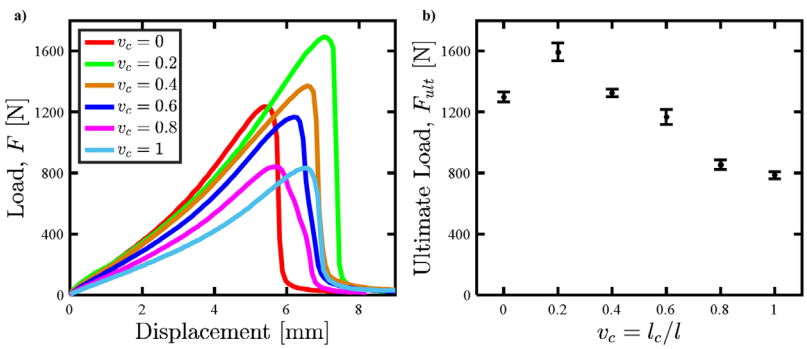

Figure 2. Performance of SLJs with different amounts of compliance-tailoring: a) Representative load-displacement curves as a function of volume fraction (ν_c) of compliant-bond in the bondlayer, and b) Ultimate load (F_{ult}) with standard error of each SLJ type as a function of compliant-bond volume fraction, ν_c.

Table 1. Summary performance of 3D printed single-lap joints.

Bondlayer design, $\nu_c = l_c/l$	Joint stiffness (N/mm)	Ultimate load (N)	Deflection at break (mm)	Joint toughness ($\times 10^3$ N*mm)
$\nu_c = 0$ (stiff)	173.52 ± 1.1	1298.40 ± 31.48	5.93 ± 0.27	3.56 ± 0.27
$\nu_c = 0.2$	173.44 ± 5.92	1594.63 ± 58.09	6.68 ± 0.19	4.89 ± 0.23
		+23% versus $\nu_c = 0$	+13% versus $\nu_c = 0$	+37% versus $\nu_c = 0$
	+88% versus $\nu_c = 1$	+103% versus $\nu_c = 1$	+5% versus $\nu_c = 1$	+59% versus $\nu_c = 1$
$\nu_c = 0.4$	155.8 ± 1.05	1324.97 ± 24.39	6.48 ± 0.13	3.90 ± 0.13
$\nu_c = 0.6$	133.04 ± 2.45	1166.57 ± 48.76	6.42 ± 0.27	3.39 ± 0.29
$\nu_c = 0.8$	112.98 ± 1.06	854.07 ± 32.03	5.82 ± 0.088	2.26 ± 0.045
$\nu_c = 1$ (compliant)	92.03 ± 1.05	784.37 ± 23.95	6.38 ± 0.093	2.24 ± 0.078

Changes (shown in red) are calculated versus the stiff and compliant constant modulus bondlayer joints, and only statistically significant increases are shown.

compared to those of the stiff joint (the top row of Figure 3). The compliance-tailored bondlayer joint (the middle row of Figure 3) strain distributions are intermediate to the two extremes (constant modulus stiff and compliant) as expected. Optical strain mapping at higher loads, closer to failure, failed due to the large strains, and appearance of cracks and shear bands in the images (see supporting video SV1).

Experimentally, the highest performing SLJ is observed to have a short ($\nu_c = 0.2$ bondlayer) compliant bond at the ends. Finite element analyses (FEA) were conducted to better understand and elucidate the reinforcement mechanisms leading to the higher performance, specifically to explore the experimentally-identified $\nu_c = 0.2$ region as a global optimum. The developed FEMs (see Figure S2 and related discussion for details) show good agreement with less than 2% difference between predicted versus measured initial (elastic) joint stiffness (see Table S2 and related discussion). **Figure 4** shows the normalized peel and shear stress distributions in the bondlayer at a loading of 300 N (See Figure 2a) along the bondlength at $y = 1.4$ mm near the top interface ($y = 1.5$ mm) as a function of ν_c, as well as the trend of maximum values for each. The peel and shear stress concentrations in Figure 4b and d follow expected trends for the constant modulus cases, for example, the profiles for the stiff ($\nu_c = 0$) and compliant ($\nu_c = 1$) constant modulus cases are nearly identical due to the relatively small change in modulus between those two cases relative to the stiff adherends. Further, the stress peaks occur at the ends ($\pm l$) of the bondlayer, with the stress peaks reduced slightly for the constant modulus compliant versus stiff bondlayer. For the compliance-tailored bondlayer cases, we observe a reduction in peak stresses (peel stress is exemplary in Figure 4b) as the compliant bond is added (increasing ν_c), with the peak location occurring at the interface of the stiff and compliant vertical interface. The reduction in peak stress is non-monotonic toward the compliant constant modulus bondlayer case (see Figure 4c). For relatively small additions of compliant-bond, the peak stress (particularly peel) reaches a local minimum at $\approx \nu_c = 0.1$. Both the maximum peel and shear stresses are minimum over $0 < l_c/l \leq 0.2$, consistent with the structural testing observations discussed earlier. The trends in maximum stress values in Figure 4c and e indicate that the compliant constant modulus case is nearly optimal for shear stress, but analysis of the peel stress distribution reveals that both have a minimum at $\approx \nu_c = 0.1$, rather than at $\nu_c = 1$. The constant modulus compliant bondlayer also will have a significantly reduced joint stiffness, as observed in the experimental data (see Table 1). Thus, from this stress analysis, the joint with $\nu_c = 0.1$ is predicted to be the

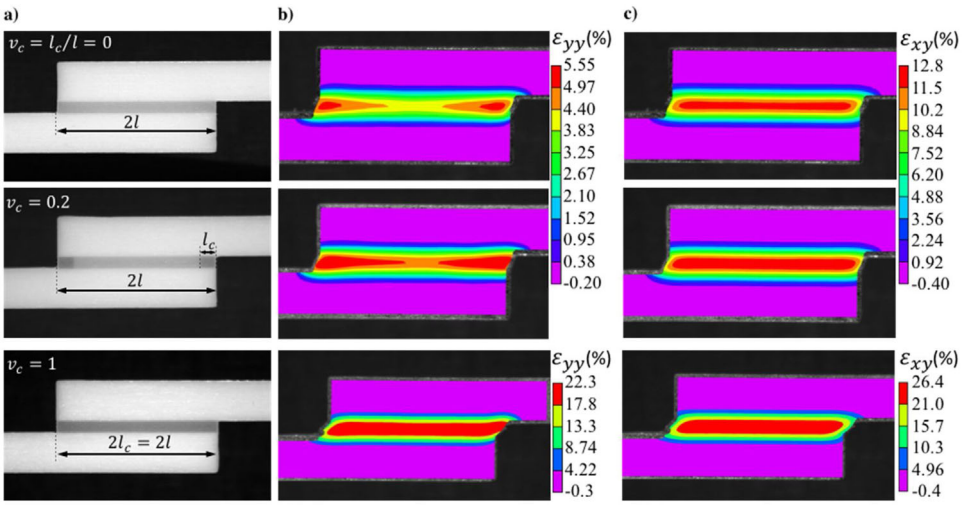

Figure 3. Strain field distribution in 3D printed SLJs for different ν_c under tensile load by DIC at 300 N (see Figure 2a): a) optical images of the SLJs, b) peel strain ε_{yy}, and c) tensorial shear strain ε_{xy}. Note that the legend scale changes for $\nu_c = 1$. l_c is the length of the compliant-bond corresponding to ν_c.

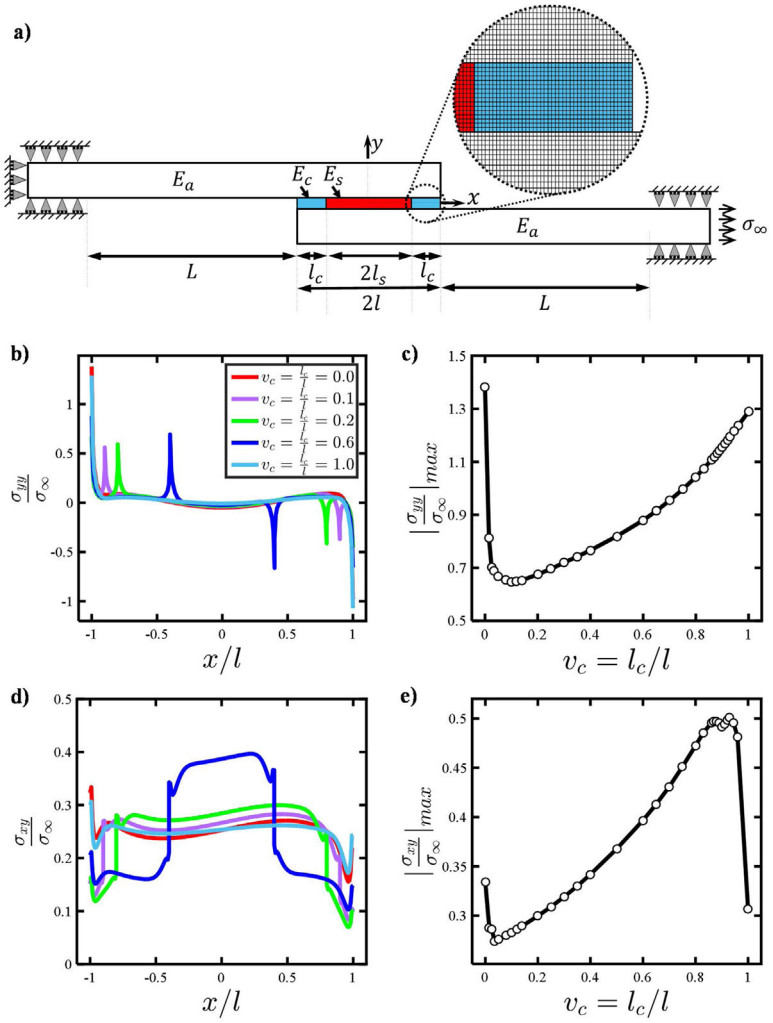

Figure 4. SLJ stress analysis in the bondlayer via *FEA*: a) Finite element (FE) model of 3D-printed SLJ with various bondlayers under far field tensile stress σ_∞, including the refined FE mesh in the stress concentration zone. E_c is the modulus of the compliant bondlayer, E_s is the modulus of the stiff bondlayer, and E_a is the modulus of the adherends. Recall that $E_s/E_c \cong 2$, and $E_a/E_s \cong 1000$. Computed stresses in the SLJ bondlayer for experimentally-tested SLJ configurations at a loading of 300 N (See Figure 2a) along the bondlength at $y = 1.4$ mm (near the top interface where $y = 1.5$ mm) as a function of v_c: b) normalized peel stress distribution, c) normalized absolute maximum peel stress, d) normalized shear stress distribution, and e) normalized absolute maximum shear stress.

highest performing across three of the four important SLJ mechanical performance metrics, consistent with the experimental findings. The fourth metric, joint toughness, involves detailed failure modeling in the context of material hysteresis and non-linearity during the failure process (see supporting video SV1). This is considered out of scope for the current work, experimental toughness is noted to be highest in the same $v_c = 0.2$ compliance-tailored bondlayer configuration (see Table 1).

Returning to joint failure and toughness trends, two characteristic failure modes were observed in the compliance-tailored SLJs studied here (see **Figure 5**): 1) cohesive failure in the bondlayer via a macroscopic shear crack (typically in the stiffer bond) and/or fine bondlayer microcracking near to final failure (typically also in the more compliant bond, and occurring over a relatively large portion of the bondlength), and 2) bondlayer peel failure. Figure 5 shows the deformation and failure behavior of SLJs with different v_c at different stages of loading unto failure. Representative optical failure images from testing, time-synched with the load-deflection plots, are provided in Figure S5 and can be viewed in supporting video, SV1, with a snapshot presented as Figure S5. The specifics of failure of this model 3D printed tri-layered assembly are not the focus of this study, but it should be noted that material properties of the bondlayer apart from modulus (that drives the stress and strain concentration reduction) such as toughness, strength, and adhesion to each other and the adherend, will also influence joint failure and toughness here. The comparisons in the experimental test matrix to the stiff and compliant constant modulus cases (see Table 1) mitigate this interpretation issue substantially, and no major differences in failure mode are observed in the compliance-tailored bondlayer cases, so these effects on toughness and strength are considered small. Furthermore, recent work with a similar single-lap joint assembly where the adhesive properties between the bondlayer and the adherend were maintained (via embedding compliant features that reduce compliance in an average sense), also created enhanced strength and toughness.[5] The features in the prior work complicate somewhat the interpretation of the direct effects of the compliance-driven mechanics by introducing other failure modes and toughening mechanisms, whereas the current work focuses solely and clearly on compliance effects. Last, it should be noted that failure initiation is also highest for the same $v_c = 0.2$ compliance-tailored bondlayer configuration, as observed in Figure 5a. Regardless of the failure mode(s) and trajectory, the stress and strain redistribution is expected to play the critical role on the joint toughness and seems to follow the same trend as strength (see earlier discussion).

The manner in which a multi-material joint carries load is strongly influenced by the overlap length relative to a critical length, usually related to the shear-lag length. The critical length is the overlap length that is needed to fully transfer the tensile load in the adherends across the bondlayer in a purely shear mode, and is the preferred approach if not limited by other constraints. An indication of this ($l \geq l_{\text{crit}}$) is that the shear stress at the center of the bondlength ($x = 0$) goes to zero. In Figure 4d, we can see that the SLJs considered thus far have $l < l_{\text{crit}}$. Cases where $l < l_{\text{crit}}$ are common in many engineering applications, where the overlap length is limited by other considerations, such as fabrication or application physical constraints.[47,48] It is known[20,49] that generally, SLJs with $l < l_{\text{crit}}$ are more prone to peel-stress driven failures due to higher peel stresses than in a comparable joint with $l > l_{\text{crit}}$. Therefore, it is of interest to also explore cases

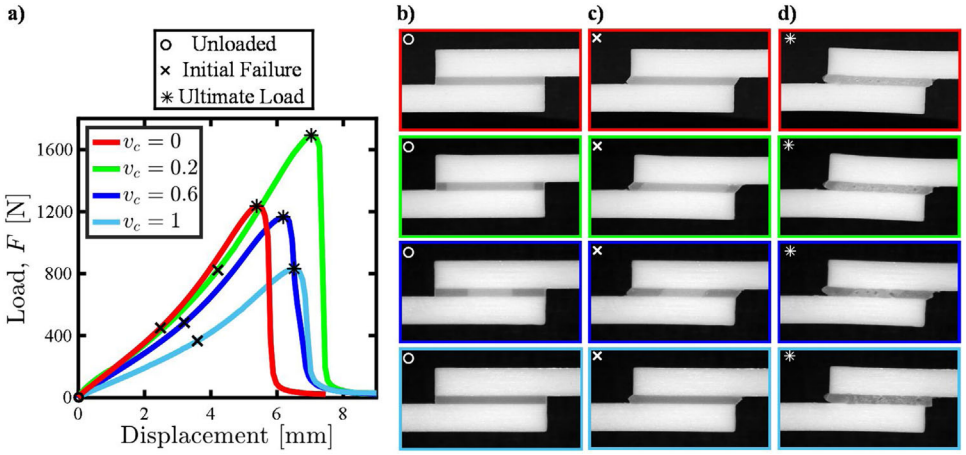

Figure 5. Failure behavior of 3D printed SLJs for different v_c: a) representative load–displacement response. Optical images of specimens at key points on the loading curve: b) unloaded, c) initial failure as identified visually, and d) near ultimate load.

with $l > l_{\text{crit}}$. The l_{crit} based on Volkersen's[50] analysis, which considers only tensile deformations of identical isotropic adherends, and shear deformation of the bondlayer, is given by

$$l_{\text{crit}} = \sqrt{\frac{E_a t_a t}{2G}} \tag{1}$$

where, E_a is the Young's modulus of the adherends, G is the shear modulus of homogeneous bondlayer, t_a is the thickness of the adherends, and t is the thickness of the bondlayer. l_{crit} scales with the modulus mismatch between adherends and bondlayer. For given adherends, high shear stiffness bondlayer reduces the critical length required for complete shear stress transfer. l_{crit} is estimated to be ≈0.3 m for the SLJs assemblies studied here using Equation 1, which is far beyond the limitations of the build platform for 3DP. Moreover, if bending deformation of adherends due to the eccentric load-path is considered, l_{crit} is ≈1 m, as observed from FEA. We, therefore, analyze the tri-layer SLJ as before (see Figure 4), but with $l = 1m > l_{\text{crit}}$. The results of the stress distributions and the maximum stress trends are shown in **Figure 6**, following the same format as Figure 4. From Figure 6a and c, we see that both peel and shear maximum stresses are reduced significantly for $l > l_{\text{crit}}$ as expected. Moreover, shear stress at the bondlayer midline is almost zero over 80% of the bondlength indicating that $l > l_{\text{crit}}$. Nevertheless, the maximum peel and shear stresses shown in Figure 6b and d indicate that the global optimum is still at $\approx v_c = 0.1$. Unlike the case where $l < l_{\text{crit}}$, the maximum peel and shear stresses in the bondlayer saturate for $l > l_{\text{crit}}$ at $v_c > 0.3$ as can be seen in Figure 6b and d, also as expected. Comparing the results from Figure 4 and 6, we note that for the short ($l < l_{\text{crit}}$) overlap case, the reduction in maximum stresses employing compliance tailoring is much greater and that the relative length (l_c/l) of compliant bond for maximum stress and strain reduction is also greater, than the long overlap case ($l > l_{\text{crit}}$). It should, however, be noted that for the single-lap configuration considered here, the joint is subjected to significant bending moment in addition to longitudinal tension on account of non-collinear load-path. Therefore, even for $l = l_{\text{crit}}$, the bondlayer is subjected to significant peel stresses at the ends of the overlap in addition to shear stresses. Therefore, failure emanates from the very end of the overlap in the bondlayer as the peel stress

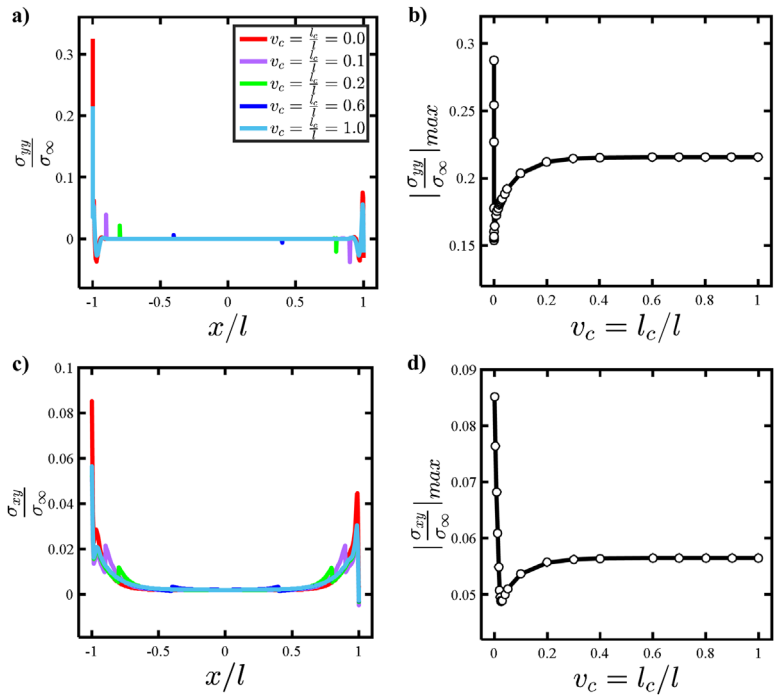

Figure 6. Computed stresses in the bondlayer for SLJs configurations with $l = 1\,m > l_{crit}$ at a loading of 300 N (See **Figure 2**a) along the bondline at $y = 1.4$ mm (near the top interface where $y = 1.5$ mm) as a function of v_c: a) normalized peel stress distribution, b) normalized absolute maximum peel stress, c) normalized shear stress distribution, and d) normalized absolute maximum shear stress.

generated exceeds the peel strength while shear stress generated in the bondlayer is still less than the shear strength of the bondlayer.

5. Conclusions

Multimaterial structural connections/joints are ubiquitous and are often preferred for lightweighting applications over mechanical methods of fastening. Strain-tolerance can be incorporated with a compliant bondlayer, but it may not have enough shear stiffness to transfer load effectively from one adherend to the other. By contrast, a stiffer bondlayer provides for a stiff joint, but may not have sufficient strain-compliance to diffuse stresses at the ends of the overlap where stresses and strains are concentrated. Compliance-tailored SLJs were fabricated combining compliant- and stiff-bonds in discrete steps along the bondlength with multi-material 3D printing to provide a graded or tailored solution. The performance of compliance-tailored joints exhibited greater than 100% increase in strength and a 60% increase in toughness for a bi-modulus case at $v_c = 20\%$ (volume fraction of compliant-bond along the bondlength) with respect to a constant modulus compliant bondlayer joint ($v_c = 100\%$), while maintaining joint stiffness versus the stiff bondlayer ($v_c = 0\%$). This synergetic effect can be explained by the stress and strain distributions in the bondlayer at and near failure, for both the cases, where the overlap length is less than (experimentally-realized) and greater than a critical value (for full load transfer in shear). Complementary FEA predictions of stress and strain redistribution are in good agreement with strain fields obtained experimentally. Both the FEA and experimental results suggest an optimal length ratio or volume fraction of compliant-bond of the bondlayer as a design parameter that enhances the mechanical behavior of joints. This study demonstrates 3D printing as a means to create high performance interface compliance-tailored joints. If the correct levels of spatial-tailoring (both properties and scale) in the bondlayer can be achieved, for example, in structural composite adhesive joining, performance may approach what some have called optimal design of such interfaces by bio-mimicking.[33,51–58] While the tailoring considered here imparts large improvements to the multilayer, even a small design improvement of such joints in application can lead to large benefits, for example, the 2017 GMC Acadia sport utility vehicle is 700 pounds lighter than the version it replaced, contributing a 28% improvement in gas mileage, due primarily to the use of improved joining materials.[48] Compliance-tailoring of the bondlayer is an additional and facile approach to improving joint performance in both short and long, relative to critical shear transfer length, bonding applications.

Supporting Information

Supporting information is available online from Wiley Online Library or from the author.

Acknowledgement

We gratefully acknowledge financial support from the ADNOC/GASCO under Award No: EX2016-000010.

Conflict of Interest

The authors declare no conflict of interest.

Keywords

Compliance-tailoring, Composite interfaces, Interface-tailoring, Multilayered materials, 3D printing

Received: October 4, 2017
Revised: October 4, 2017
Published online: November 8, 2017

[1] S. Suresh, *Science* **2001**, *292*, 2447.
[2] P. Katti, S. Bose, S. Kumar, *Polymer (Guildf)* **2016**, *102*, 43.
[3] A. P. Awasthi, M. E. Grady, I. H. Kim, N. R. Sottos, P. H. Geubelle, *Mech. Mater.* **2016**, *98*, 71.
[4] S. Tamrakar, Q. An, E. T. Thostenson, A. N. Rider, B. Z. (Gama) Haque, J. W. Gillespie, *ACS Appl. Mater. Interfaces* **2016**, *8*, 1501.
[5] S. Kumar, B. L. Wardle, M. F. Arif, *ACS Appl. Mater. Interfaces* **2017**, *9*, 884.
[6] V. Tvergaard, J. W. Hutchinson, *J. Mech. Phys. Solids* **1996**, *44*, 789.
[7] K. Matous, M. G. Kulkarni, P. H. Geubelle, *J. Mech. Phys. Solids* **2008**, *56*, 1511.
[8] T. Hirano, K. Wakashima, *MRS Bull.* **1995**, *20*, 40.
[9] R. L. Williamson, B. H. Rabin, J. T. Drake, *J. Appl. Phys.* **1993**, *74*, 1310.
[10] A. E. Giannakopoulos, S. Suresh, M. Finot, M. Olsson, *Acta Metall. Mater.* **1995**, *43*, 1335.
[11] N. Wang, S. Xia, *J. Mech. Phys. Solids* **2017**, *98*, 87.
[12] M. Goland, E. Reissner, *J. Appl. Mech.* **1944**, *11*, A17.
[13] J. N. Boss, V. K. Ganesh, C. T. Lim, *Compos. Struct.* **2003**, *62*, 113.
[14] J.-S. Kim, C.-G. Kim, C.-S. Hong, *Compos. Struct.* **2001**, *51*, 285.
[15] J. Y. Cognard, R. Créac'hcadec, J. Maurice, *Int. J. Adhes. Adhes.* **2011**, *31*, 715.
[16] A. R. Rispler, L. Tong, G. P. Steven, M. R. Wisnom, *Int. J. Adhes. Adhes.* **2000**, *20*, 221.
[17] M. Y. Tsai, J. Morton, *Compos. Struct.* **1995**, *32*, 123.
[18] J. Rion, Y. Leterrier, J.-A. E. Månson, *Compos. Part A Appl. Sci. Manuf.* **2008**, *39*, 1547.
[19] C. Raphael, *Appl. Polym. Symp.* **1966**, *3*, 99.
[20] L. J. Hart-Smith, *Adhesive-Bonded Single-Lap Joints*, Langley Research Center, Hampton, VA **1973**.
[21] S. Srinivas, *Analysis of Bonded Joints*, NASA Langley Research Center, Hampton, VA **1975**.
[22] J. F. Durodola, *Int. J. Adhes. Adhes.* **2017**, *76*, 83.
[23] S. Kumar, R. D. Adams, *Int. J. Adhes. Adhes.* **2017**, *76*, 1.
[24] S. Kumar, *Int. J. Adhes. Adhes.* **2009**, *29*, 785.
[25] S. Kumar, *in Advances in Modeling and Design of Adhesively Bonded Systems*, Wiley-Scrivener **2013**, p. 47.
[26] S. E. Stapleton, A. M. Waas, S. M. Arnold, *Int. J. Adhes. Adhes.* **2012**, *35*, 36.
[27] N. Stein, P. Weißgraeber, W. Becker, *Int. J. Solids Struct.* **2016**, *97–98*, 300.
[28] N. Stein, H. Mardani, W. Becker, *Int. J. Adhes. Adhes.* **2016**, *70*, 117.
[29] N. W. Bartlett, M. T. Tolley, J. T. B. Overvelde, J. C. Weaver, B. Mosadegh, K. Bertoldi, G. M. Whitesides, R. J. Wood, *Science* **2015**, *349*, 161.
[30] L. S. Dimas, G. H. Bratzel, I. Eylon, M. J. Buehler, *Adv. Funct. Mater.* **2013**, *23*, 4629.
[31] J. O. Hardin, T. J. Ober, A. D. Valentine, J. A. Lewis, *Adv. Mater.* **2015**, *27*, 3279.

[32] I. Roppolo, A. Chiappone, A. Angelini, S. Stassi, F. Frascella, C. F. Pirri, C. Ricciardi, E. Descrovi, *Mater. Horiz*. **2017**, *4*, 396.
[33] B. G. Compton, J. A. Lewis, *Adv. Mater.* **2014**, *26*, 5930.
[34] A. R. Studart, *Adv. Funct. Mater.* **2013**, *23*, 4423.
[35] M. Hofmann, *ACS Macro Lett*. **2014**, *3*, 382.
[36] A. A. Martin, M. Toth, I. Aharonovich, *Sci. Rep*. **2014**, *4*, 5022.
[37] K. Sun, T.-S. Wei, B. Y. Ahn, J. Y. Seo, S. J. Dillon, J. A. Lewis, *Adv. Mater.* **2013**, *25*, 4539.
[38] J. Liljenhjerte, P. Upadhyaya, S. Kumar, *Addit. Manuf.* **2016**, *11*, 40.
[39] Y. Jo, J. Y. Kim, S.-Y. Kim, Y.-H. Seo, K.-S. Jang, S. Y. Lee, S. Jung, B.-H. Ryu, H.-S. Kim, J.-U. Park, Y. Choi, S. Jeong, *Nanoscale* **2017**, *9*, 5072.
[40] R. O. Ritchie, *Nat. Mater.* **2011**, *10*, 817.
[41] L. Wang, J. Lau, E. L. Thomas, M. C. Boyce, *Adv. Mater.* **2011**, *23*, 1524.
[42] E. Lin, Y. Li, C. Ortiz, M. C. Boyce, *J. Mech. Phys. Solids* **2014**, *73*, 166.
[43] P. Upadhyaya, S. Kumar, *Mech. Mater.* **2015**, *89*, 190.
[44] I. Pires, L. Quintino, J. F. Durodola, A. Beevers, *Int. J. Adhes. Adhes*. **2003**, *23*, 215.
[45] L. F. M. da Silva, R D Adams, *Int. J. Adhes. Adhes*. **2007**, *27*, 227.
[46] L. F. M. da Silva, M. J. C. Q. Lopes, *Int. J. Adhes. Adhes*. **2009**, *29*, 509.
[47] M. Davis, D. Bond, *Int. J. Adhes. Adhes*. **1999**, *19*, 91.
[48] N. E. Boudette, "The Superglue Diet: How to Make a Lighter, Fuel-Sipping Car," can be found under https://www.nytimes.com/2016/08/12/automobiles/the-superglue-diet-how-to-make-a-lighter-fuel-sipping-car.html, **2016**.
[49] S. Kumar, K. L. Mittal, Eds., *Advances in Modeling and Design of Adhesively Bonded Systems*, Wiley-Scrivener, **2013**.
[50] O. Volkersen, *Luftfahrtforschung* **1938**, *15*, 41.
[51] S. Deville, *Science* **2006**, *311*, 515.
[52] C. Ortiz, M. C. Boyce, *Science* **2008**, *319*, 1053.
[53] E. Munch, M. E. Launey, D. H. Alsem, E. Saiz, A. P. Tomsia, R. O. Ritchie, *Science* **2008**, *322*, 1516.
[54] A. Miserez, T. Schneberk, C. Sun, F. W. Zok, J. H. Waite, *Science* **2008**, *319*, 1816.
[55] J. Han, Y. Dou, D. Yan, J. Ma, M. Wei, D. G. Evans, X. Duan, *Chem. Commun*. **2011**, *47*, 5274.
[56] F. Barthelat, *J. Mech. Phys. Solids* **2014**, *73*, 22.
[57] M. Bacca, J. A. Booth, K. L. Turner, R. M. McMeeking, *J. Mech. Phys. Solids* **2016**, *96*, 428.
[58] F. Libonati, M. J. Buehler, *Adv. Eng. Mater.* **2017**, *19*, 1600787.

Supporting Information

Stress Reduction of 3D Printed Compliance-Tailored Multilayers

S. Kumar *[,a], Brian L. Wardle[b], Muhamad F. Arif[a], Jabir Ubaid[a]

[a]Department of Mechanical and Materials Engineering, Masdar Institute, Masdar City, P.O. Box 54224, Abu Dhabi, UAE

[b]Department of Aeronautics and Astronautics, Massachusetts Institute of Technology, Cambridge, MA 02139, USA

* Corresponding author. Fax: +971 2 8109239.

Email address: s.kumar@eng.oxon.org, skumaar@mit.edu (S. Kumar)

Geometrical Properties and Loads

A SLJ, even if subjected to a simple tension, experiences bending moments and transverse shear forces as shown in Figure S1. Goland and Reissner[12] accounted for the rotation of the joint due to such non-collinear load path and provided analytical expressions for both shear and peel stress concentrations in the bondlayer, assuming that both stresses vary only as a function of x over the bondlength.

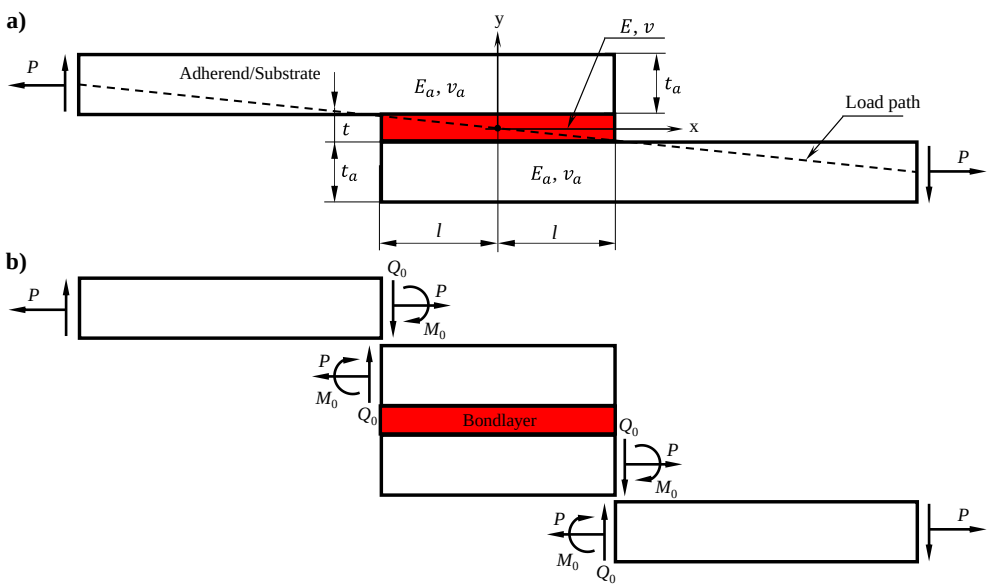

Figure S1. Single-lap joint with identical adherends (after[12]): a) Eccentric load-path due to tensile load P, b) additional bending moment and transverse shear force at the ends of the overlap due to rotation of the joint.

Normalized shear stress bondlayer is given by:

$$\frac{\tau(x)}{\sigma_\infty} = \left(\frac{-1}{8}\right)\left(\frac{t_a}{l}\right)\left\{\frac{\beta l}{t_a}(1+3k)\frac{\cosh\left(\frac{\beta l}{t_a}\frac{x}{l}\right)}{\sinh\left(\frac{\beta l}{t_a}\right)} + 3(1-k)\right\}$$

where σ_∞ is the applied tensile stress and k is is bending moment factor given by:

$$k = \frac{\cosh(\rho l)}{\cosh(\rho l) + 2\sqrt{2}\sinh(\rho l)}$$

where $\rho = \sqrt{\frac{3(1-\nu_a{}^2)}{2}}\frac{1}{t_a}\sqrt{\frac{P}{t_a E_a}}$ and $\beta^2 = 8\frac{G}{E_a}\frac{t_a}{t} = \frac{4Et_a}{E_a t(1+\nu)}$.

Normalized peel stress in the bondlayer, $\sigma(x)$ is given by:

$$\frac{\sigma(x)}{\sigma_\infty} = \frac{1}{\Delta}\left(\frac{t}{l}\right)^2\left\{\left(R_2\lambda^2\frac{k}{2} + \lambda k' \quad \cosh\lambda\cos\lambda\right)\cosh\left(\frac{\lambda x}{l}\right)\cos\left(\frac{\lambda x}{l}\right)\right.$$
$$\left. + \left(R_1\lambda^2\frac{k}{2} + \lambda k' \quad \sinh\lambda\sin\lambda\right)\sinh\left(\frac{\lambda x}{l}\right)\sin\left(\frac{\lambda x}{l}\right)\right\}$$

where k' is transverse force factor given by:

$$k' = \frac{kl}{t_a}\sqrt{3(1-\nu_a{}^2)\frac{P}{t_a E_a}}$$

and $\lambda = \gamma\frac{l}{t_a}$; $\gamma^4 = \frac{6E(1-\nu_a{}^2)}{E_a}\frac{t_a}{t}$; $\Delta = \frac{1}{2}(\sinh(2\lambda) + \sin(2\lambda))$; $R_1 = \cosh\lambda\sin\lambda + \sinh\lambda\cos\lambda$; and $R_2 = \sinh\lambda\cos\lambda - \cosh\lambda\sin\lambda$.

Figure S2 shows the dimensions of the 3D printed compliance-tailored SLJ specimens for tensile testing up to failure. Spacers and grip locks are required for easier mounting and axial loading during testing in the Zwick Roell tensile testing machine.

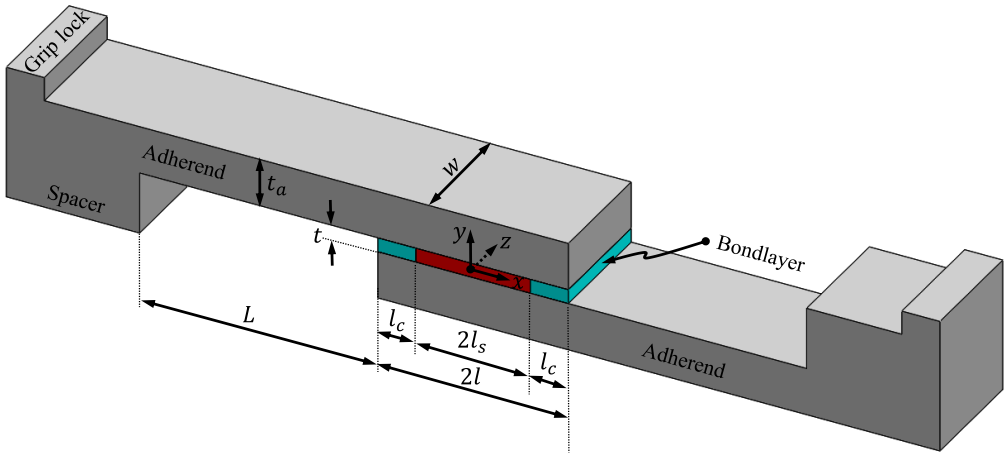

Figure S2. Geometrical configuration of 3D printed compliance-tailored joints. $L = 50$ mm, $2l = 40$ mm, $t = 3$ mm, $t_a = 10$ mm and $w = 20$ mm. l_c and l_s are the length portion of the compliance- and stiff-bond, respectively.

Material characterization

The stress-strain response for the adherend/substrate and bondlayer materials are provided in Figure S3. Linear elastic properties of the materials VW, S60 and S40 are determined as per ASTM D412. Dog bone samples of VW, S60 and S40 with gauge length of 25mm, width of 6mm and thickness of 2 mm are printed using the same Object Connex260 3D printer. In order to perform Digital Image Correlation (DIC), the samples are coated with white acrylic paint and then

random speckles are generated on the white paint by spraying black acrylic paint using an air brush. Uniaxial tensile tests are performed using Zwick-Roell universal testing machine at a constant cross head speed of 5mm/minute. While the specimen is being loaded, images of the speckle pattern on the surface of the specimen are captured using a 5.0 MP CCD camera. The load, F during the tensile tests is recorded using a 2.5 kN load cell and the engineering stress, σ_{xx-eng} is calculated with respect to the original cross-sectional area (A_0) such that $\sigma_{xx-eng} = F/A_o$. Engineering surface strains in loading direction (ε_{xx-eng}) and in lateral direction (ε_{yy-eng}) are computed by digital image correlation using Vic-2D software. Elastic moduli for all the samples are determined by calculating the initial slope of the engineering stress – engineering strain curves. Poison's ratio (ν) for all the samples are found out by calculating the initial slope of $-\varepsilon_{yy-eng}$ vs. ε_{xx-eng} curves. The materials properties determined are listed in Table S1.

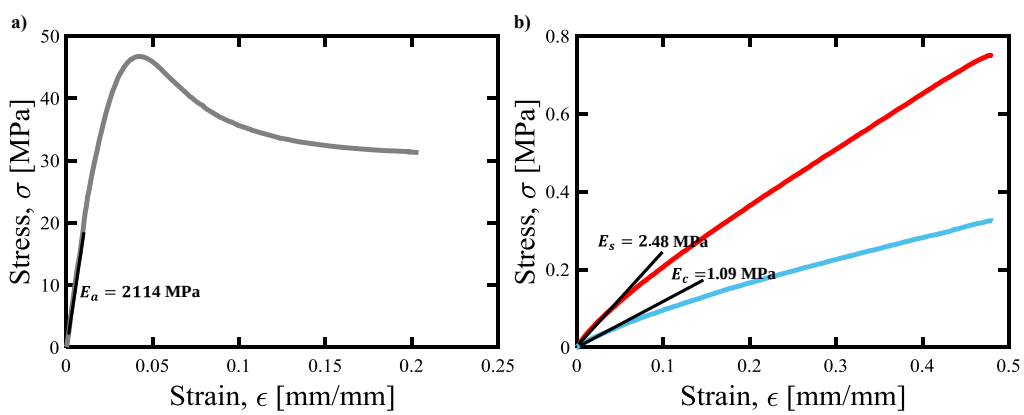

Figure S3. Stress-strain response of 3D printed adherend and bondlayer materials under tensile loading. $E_a \gg E_s \cong 2E_c$. E_a, E_s and E_c corresponds to

the Young's Modulus of the adherend, stiff bondlayer, and compliant bondlayer, respectively.

Table S1. Elastic properties of 3D printed materials used for the SLJ

Joint Material	Young's Modulus (MPa)	Poisson Ratio
Adherend (VeroWhite)	2114	0.336
Stiff bondlayer (Shore60)	2.48	0.491
Compliant bondlayer (Shore40)	1.09	0.493

FEA Validation vis-à-vis Experiments

The initial macroscopic load-displacement response of the joint obtained from the FEA is compared with experimental results for $v_c = 0.0, 0.2, 0.6$ and 1.0 as shown in Figure S4. Figure S4 demonstrates that the FE model captures the mechanical response of the joint accurately until ~ 600 N load level up to which the system behaves in a neo-Hookean manner. Beyond this load level, damage initiation and its evolution with load may lead to divergence in response as the FE model employed does not capture the damage/failure progression. Table S2 shows the initial stiffness of joints obtained both from FEA and experiments as a function of $v_c = l_c/l$, showing generally good agreement. In the main text, the FE analyses presented in the next section will focus on capturing the linear elastic behavior at a load level of 300 N to study the redistribution of stress and strain fields due to compliance-tailoring of the bondlayer.

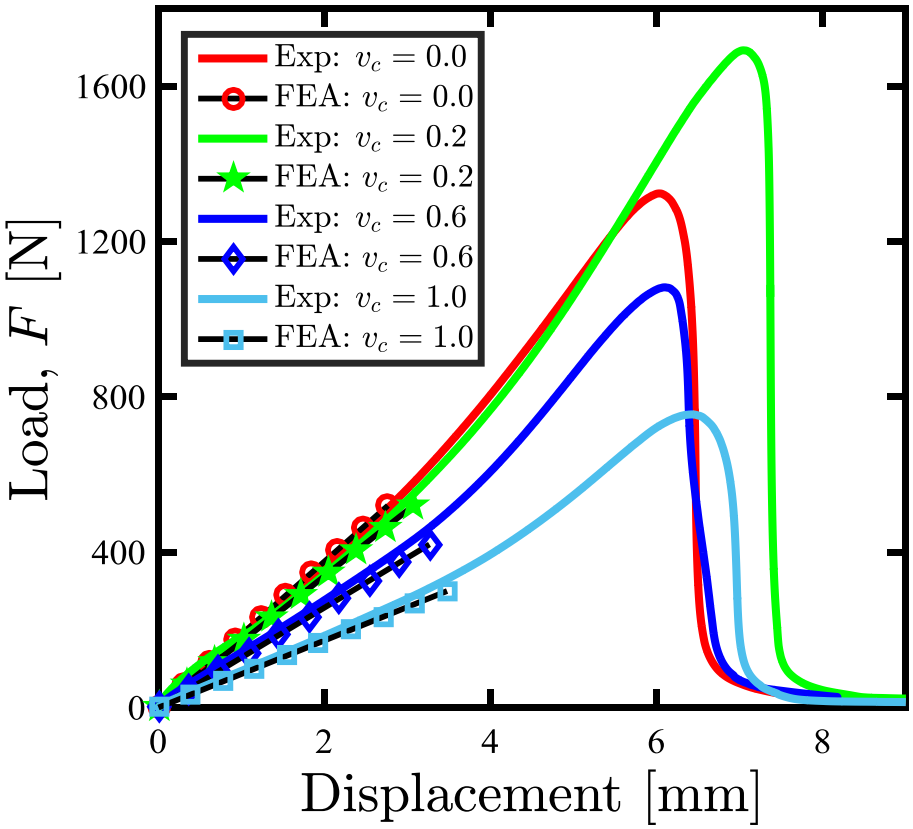

Figure S4. FEA (up to 600 N) vs. experiment of compliance-tailored joint load-deflection response for joints with varying v_c.

Table S2. FEA vs. experiments: Macroscopic stiffness of the joints as a function of v_c.

Design Configuration $v_c = l_c/l$	Joint stiffness from experiment (N/mm)	Joint stiffness from simulation (N/mm)	Difference (%)
$v_c = 0$	173.52 ± 1.1	188.19	8.45
$v_c = 0.2$	173.44 ± 5.92	169.35	-2.36
$v_c = 0.4$	155.8 ± 1.05	149.25	-4.20
$v_c = 0.6$	133.04 ± 2.45	128.68	-3.28
$v_c = 0.8$	112.98 ± 1.06	107.53	-4.82
$v_c = 1$	92.03 ± 1.05	86.29	-6.24

Failure of the Joints

The compliance-tailored joint system allows for more of the load transfer to occur away from the high stress concentration ends in the stiffer middle part of the bondlayer, and failure trends (see main text) for both initiation and ultimate failure follow the trends for maximum stress as v_c is varied. The contribution of the stiff and compliant bonds can also be seen from the failure progression of the joints in supplemental video SV1, with a snapshot near final failure for the $v_c = 0.2$ configuration in Figure S5.

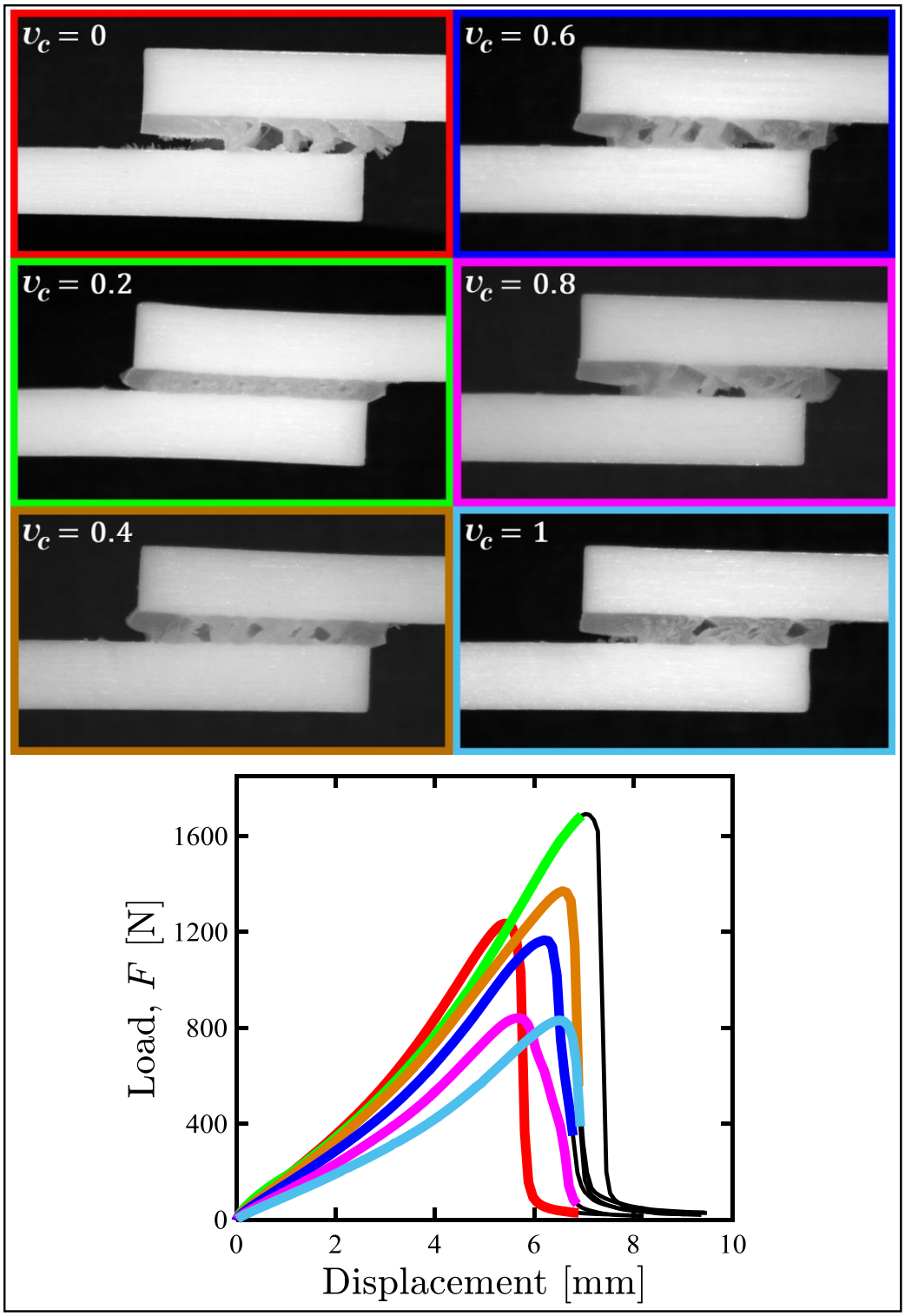

Figure S5. Representative optical failure images from testing, time-synched with the load-deflection plots for different v_c.